Wave generation through the interaction of a mode-2 internal solitary wave and a broad, isolated ridge

David Deepwell,[1,*] Marek Stastna,[2] Magda Carr,[3] and Peter A. Davies[4]
[1]*Department of Physics, University of Alberta, Edmonton, Canada*
[2]*Department of Applied Mathematics, University of Waterloo, Waterloo, Canada*
[3]*School of Mathematics, Statistics and Physics, Newcastle University, Newcastle upon Tyne, United Kingdom*
[4]*Department of Civil Engineering, University of Dundee, Dundee, United Kingdom*

(Received 14 May 2019; published 16 September 2019)

The passage of a mode-2 internal solitary wave (ISW) over a broad, isolated ridge was explored using both numerical simulations and laboratory experiments. At sufficient incident wave amplitude and speed, the interaction with the ridge caused a deceleration of the incident wave while also generating three wave types: leading mode-1 ISWs, a trailing mode-1 wave-packet, and a trailing mode-2 ISW. The trailing mode-2 ISW was formed as the second piece of the fissioned incident wave. While mode-mode interactions are not part of typically applied weakly nonlinear theories, the fissioning of the leading mode-2 ISW into two mode-2 waves is predicted qualitatively by weakly-nonlinear theory. However, the present study is, to our knowledge, the first experimental and numerical confirmation of the detailed evolution of this phenomenon. In contrast to the previously studied transit of a mode-2 ISW onto a shelf, the parameters quantifying the strength of each resultant wave are found to be independent, having no singular predictor existing for all waves. Lastly, cross-boundary layer transport was found to be more strongly dependent on Reynolds number than on incident wave or background conditions.

DOI: 10.1103/PhysRevFluids.4.094802

I. INTRODUCTION

The interior of the world's oceans is filled with waves for which gravity is the restoring force. Some of the largest and most energetic are internal solitary waves (ISWs) which can reach amplitudes over 200 m in depths of $\mathcal{O}(1000\ \mathrm{m})$ [1]. Since the ocean typically has a well defined pycnocline near the surface that dominates the density stratification, the most commonly observed ISWs have a mode-1 structure in which isopycnals rise and fall together at all depths. However, the last decade has seen a growth in the interest for, and number of observations of [2–5], mode-2 ISWs which have isopycnals that expand away and contract towards the pycnocline center.

Until quite recently, almost all numerical and experimental studies of mode-2 ISWs had been idealized studies with pycnoclines located at the mid-depth [6–10]; these focused on wave properties such as the dependence of wave speed and wavelength on amplitude, and the ability of the waves to transport mass. More recently, interest has shifted to how mode-2 ISWs are influenced by external conditions such as pycnocline location [11], changing layer depths [12–16], or a shear layer [17].

Yuan, Grimshaw, and Johnson [14] used both theory [a variable-coefficient Korteweg–de Vries (vKdV) equation] and modeling (with the MITGCM) to investigate how a mode-2 ISW adjusts when

*deepwell@ualberta.ca

propagating onto a slope-shelf topography in a three-layer stratification for which the bottom-most pycnocline may disappear due to a decrease in total depth. Two main comparisons were made: (1) where the fluid went from a three-layer system to either a three-layer system or a two-layer system on the shelf and (2) whether the nonlinear coefficient changed sign or not. The authors found a small transfer of energy from mode-2 into mode-1 internal waves when the fluid remains a three-layer system as it shoals, even after the initial mode-2 ISW changes polarity, or the wave passes the point at which the nonlinear coefficient changes sign. When the stratification was reduced to two layers on the shelf, the mode-2 wave completely transitioned into a mode-1 bore, as expected. The authors suggested that mode-2 ISWs shoal in a manner similar to mode-1 ISWs with the exception that shoaling mode-2 ISWs may generate mode-1 waves, thereby complicating the wave field. No attempt to accurately resolve the bottom boundary layer was made (i.e., the Leith viscosity as implemented in the MITGCM was used).

Similarly, Terletska *et al.* [12] explored how a bottom step topography permanently modifies an incident mode-2 ISW. Depending on the height of the step and the wave amplitude, not only were mode-1 ISWs generated, but in many cases an internal wave packet of the first mode (sometimes referred to as a breather-like wave [18]) was formed.

Though only a single publications exists on mode-2 ISWs traveling over a ridge (Deepwell *et al.* [13]), this is not a new topic for internal waves of the first mode. It has been shown that wave breaking [19], generation of higher mode waves, and wave reflection [20] are possible. Lamb and Warn-Varnas [21], in the context of the well studied South China Sea, explored the role of bathymetric bumps on the shoaling of mode-1 ISWs. The authors found that bumps in deep water, well away from the stratification, have little effect, while shallower bumps profoundly effect the nature of mode-2 wave generation. In particular, both convex and concave mode-2 waves are generated by the bump. This suggests that isolated topography may have important effects on wave evolution even when no terminal shoaling (i.e., shoaling during which the incident wave is completely destroyed) occurs.

To summarize, all previous mode-2 shoaling studies we are aware of, except for Deepwell *et al.* [13], have been interested in an ISW traveling onto a shelf, a slope, or a combination of the two. Here, as in Deepwell *et al.* [13], we will shift attention to the transit of a mode-2 internal solitary wave over a broad ridge rather than onto a shelf. The reasons for this are threefold: (1) internal solitary waves may interact with submarine ridges in the ocean causing local changes that may have ecological implications [22]; (2) to investigate the partial fragmentation of the incident mode-2 ISW into internal waves of other modes; and (3) to understand the long-term impacts that a short-duration change in environmental conditions has on the form and speed of the ISW that emerges from the interaction. This is particularly important for understanding the different pathways of energy conversion between scales, in contrast to the usual discussion of energy cascading from large to small scales. Observations for both types of energy conversion have been made on the New Jersey coast where a shoaling mode-2 wave radiated energy into a mode-1 wave tail and turbulent dissipation [5]. As a result of these conversions, the incident wave was short-lived and it was unclear how to predict the duration and change of the waveform from the background conditions. It is also important that the topography is broader than the sharp changes considered by past authors, whether in the context of ridges (Deepwell *et al.* [13]) or shelves (Terletska *et al.* [12]), while maintaining high resolution in the thin boundary layer region.

Given that we focus on a situation in which the incident wave is expected to survive, to at least some degree, during the shoaling, it is worth reviewing the possibility of theoretical descriptions. When the bathymetry varies slowly, perturbation theory allows for the derivation of various weakly nonlinear (WNL) models, which partially represent the effects of finite amplitude (nonlinearity) and finite wavelength (dispersion). WNL theories have occupied multiple authors over several decades. The recent article by Lamb and Xiao [23] has, to our knowledge, the most complete comparison of variable coefficient WNL theories with numerical simulations of the full governing equations. Lamb and Xiao [23] find that while all WNL theories make some phase and amplitude errors, what they called the GardnerII equation performs the best. There are two caveats relevant to the present

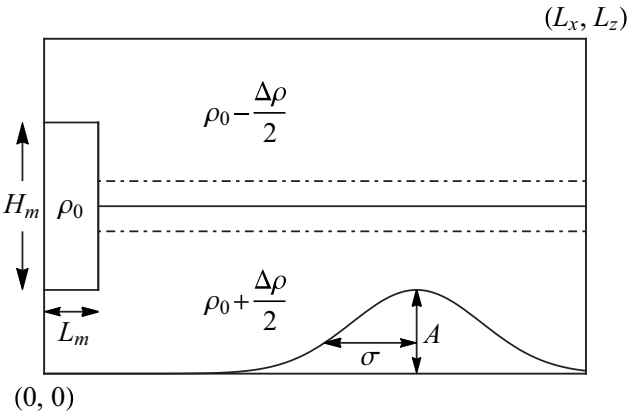

FIG. 1. Initial tank configuration (side view). Horizontal lines denote the location of the pycnocline center (solid line), and pycnocline half-width (semidashed lines). The intermediate region with height H_m and width L_m contains density ρ_0 and is centered on the pycnocline (left end of tank). Modified from Deepwell *et al.* [13].

discussion. First, Lamb and Xiao [23] consider only pseudo-two-layer stratifications and mode-1 waves. Second, the theory, by construction, precludes any interaction between different modes. So-called multimode WNL theories are available, with a particularly relevant example being that discussed in Gerkema [24]. Gerkema's oceanic case studies, however, do not include a significant mode-1 component, and the form of the theory is that of the regularized long wave equation (RLW), which Lamb and Xiao [23] identify as suboptimal for a quantitative description of shoaling. In any event, while WNL may have a role to play in studying large scale phenomena in the ocean, for experimental scales such as those we consider, there is less impetus for avoiding direct numerical simulation.

The remainder of this paper is organized as follows. Section II will present the laboratory and numerical setup, in which internal solitary waves are generated, along with a diagnostic used to distinguish waves of different vertical mode. Section III will present a characterization of the incident and transmitted waves. Section IV will discuss the resultant waves formed during the wave-hill interaction. The details of the evolution, as well as the boundary layer dynamics and cross-boundary-layer transport will then be discussed in Sec. V, in addition to a comparison to shoaling over a narrow ridge. Section VI will conclude the paper.

II. METHODS

A. Experimental and numerical arrangement

We have completed both laboratory experiments and numerical simulations of mode-2 ISWs passing over a broad ridge placed on the bottom of a rectangular tank. The ISWs traveled along the pycnocline of a pseudo-two-layer fluid that is well approximated by a hyperbolic tangent profile (or rather, defined as such for numerical simulations). We focus primarily on the numerical results, while the laboratory experiments provide validation of the model and information of particle motion.

The ISWs were generated by the typical lock-release mechanism [8]. At one end of the tank a gate separates the background stratification from the intermediate region containing three layers. In this region, the density of the lower and upper layers matches that of the background, while that of the middle layer (centered on the mid-depth) is set to equal the average density of the upper and lower layers, ρ_0 (see Fig. 1). Further details of the laboratory procedures used to create the stratified ambient fluid and the intermediate fluid, in addition to the visualization techniques, are described in Deepwell *et al.* [13]. Removal of the gate releases the intermediate fluid of density ρ_0 forming a series of mode-2 ISWs.

TABLE I. Tank dimensions and ridge parameters.

Case	L_x (m)	L_y (m)	L_z (m)	A (m)	x_0 (m)	σ (m)
Num.	12.8	0.4	0.25–0.40	0.10	4.8	0.60
Expt.	6.4					

Since the pycnocline is placed at the mid-depth, any resultant mode-2 ISWs remain symmetric about the pycnocline. As a result, no mode-1 waves exist prior to interaction with the ridge. Should the pycnocline be raised or lowered, or the intermediate fluid region be offset from the pycnocline (see Carr, Davies, and Hoebers [11] and Olsthoorn, Baglaenko, and Stastna [25]), or a background shear exist [17], then mode-1 waves would form.

The ISW traveled over an isolated ridge described by the Gaussian

$$h(x) = A \exp\left[-(x - x_0)^2/\sigma^2\right],$$

where the peak of the ridge remains below the pycnocline for all cases. A summary of the tank dimensions and ridge parameters is given in Table I. The numerical domain was twice as long as the physical tank to allow for the accurate representation of fast mode-1 ISWs that form in the wave-ridge interaction. All experiments and simulations used a ridge width of $\sigma = 0.6$ m and all numerical simulations are two-dimensional.

The aspect ratio, $A/\sigma = 1/6 \approx 0.17$, is comparable (though on the high end) to some of the steepest topographical features in the ocean. The maximum slope of 0.14 is roughly half of the slope of 0.33 used in Sveen *et al.* [19] and Guo *et al.* [26] and is roughly five times smaller than that in Deepwell *et al.* [13]. Since the slope is considerably shallower than that used in Deepwell *et al.* [13], the ridge is therefore wider and will be described as broad in comparison. The step topography, used in studies like that of Terletska *et al.* [12], can be thought of as the opposite limit of our broad ridge since the depth changes discontinuously.

The mode-2 linear, long-wave speed [27]

$$c_{2,0} = \frac{1}{2}\sqrt{\frac{gd\Delta\rho}{\rho_0}}, \tag{1}$$

where d is the pycnocline half-width (the typical length scale used in a hyperbolic tangent density profile), $\Delta\rho$ is the density difference between the upper and lower layers, and ρ_0 is the average density of the two fluid layers. Though $c_{2,0}$ is often used as a characteristic velocity scale, it is inapplicable for the waves of large amplitude used in this study. Thus, the incident wave speed c_{in} and the pycnocline half-width d are used to define the Reynolds number of the incident ISW, $\text{Re} = c_{\text{in}}d/\nu$.

The parameters of the numerical simulations and experiments are listed in Table II. In summary, the fluid depth varied between 0.25 and 0.40 m, and the intermediate fluid depth varied between 0.04 and 0.12 m. Within the set of simulations, the nondimensionalized density difference was 2.3%, a value which matches well the density differences used in the laboratory experiments. The simulations used a viscosity and diffusion of 2×10^{-6} m^2/s and 2×10^{-7} m^2/s, respectively, giving a Schmidt number of 10. Though smaller than that of the salt-stratified laboratory experiment, bulk results are not affected by this discrepancy in Sc.

B. Numerical methods

Two dimensional numerical simulations were completed using the Spectral Parallel Incompressible Navier-Stokes Solver (SPINS) [28] with initial conditions equivalent to the laboratory experiments. This model solves the fully nonlinear Navier-Stokes equations under the Boussinesq approximation. No-slip boundary conditions were used in the vertical directions (top and bottom

TABLE II. Numerical and experimental parameters.

Case	L_z (m)	H_m (m)	L_m (m)	d (mm)	$\Delta\rho/\rho_0$	$c_{\text{in}}/c_{2,0}$	a_{in}/d	a_{in}/ℓ	Re
				Numerical					
2504	0.25	0.04	0.3	10	0.023	1.40	0.86	0.57	166
2506	0.25	0.06	0.3	10	0.023	1.72	1.65	1.10	205
2508	0.25	0.08	0.3	10	0.023	1.94	2.41	1.61	231
2510	0.25	0.10	0.3	10	0.023	2.08	3.09	2.06	247
3004	0.30	0.04	0.3	10	0.023	1.43	0.90	0.23	170
3006	0.30	0.06	0.3	10	0.023	1.77	1.69	0.42	210
3008	0.30	0.08	0.3	10	0.023	2.01	2.50	0.63	238
3009	0.30	0.09	0.3	10	0.023	2.10	2.79	0.70	249
3010	0.30	0.10	0.3	10	0.023	2.17	3.16	0.79	258
3012	0.30	0.12	0.3	10	0.023	2.25	3.60	0.90	267
3506	0.35	0.06	0.3	10	0.023	1.80	1.77	0.27	214
3508	0.35	0.08	0.3	10	0.023	2.05	2.49	0.38	244
3509	0.35	0.09	0.3	10	0.023	2.15	2.94	0.45	255
3510	0.35	0.10	0.3	10	0.023	2.22	3.24	0.50	264
3512	0.35	0.12	0.3	10	0.023	2.31	3.72	0.57	275
4008	0.40	0.08	0.3	10	0.023	2.08	2.57	0.29	247
4010	0.40	0.10	0.3	10	0.023	2.27	3.30	0.37	269
4012	0.40	0.12	0.3	10	0.023	2.38	3.77	0.42	282
				Experimental					
3006e	0.30	0.059	0.3	9.9	0.021	1.6	1.5	0.37	364
3010e	0.30	0.103	0.3	9.1	0.021	2.1	2.9	0.64	413
3508e	0.35	0.080	0.3	9.4	0.020	2.0	2.0	0.28	402
3510e	0.35	0.099	0.3	9.3	0.022	2.2	3.0	0.43	448
4011e	0.40	0.114	0.3	8.6	0.021	2.4	3.5	0.34	440
4014e	0.40	0.136	0.3	9.7	0.020	2.5	3.9	0.41	530

boundaries) through the use of Chebyshev grids to cluster points within the boundary layer. The free-slip condition was used in horizontal directions by using Fourier grids. The grid, and all variables, were discretized with $N_x \times N_z = 8192 \times 384$ points, giving a grid spacing of 1.56 mm in the horizontal and maximum vertical spacing of 1.23 mm near the mid-depth. Within the boundary layer, the vertical grid spacing is $\mathcal{O}(10^{-2}$ mm) due to the inherent clustering of the Chebyshev grid. This gives excellent resolution for resolving the boundary layer.

The time stepper is a variable, third-order Adams-Bashforth scheme allowing for large time steps during the initial wave propagation and smaller time steps during the dynamic wave fissioning. Should the energy cascade be improperly modeled, the energy would build at the small scales, leading to a growth in the extrema of density and velocity over time. Having checked for this, the extrema values indicate that the chosen resolution was appropriate. Time-dependent simulations were completed on the high-performance computing cluster SHARCNET [29]. The majority of the subsequent results are from the numerical simulations.

C. Internal wave mode characterization

By assuming that the x axis corresponds to the direction of propagation, the linear theory of vertically trapped internal waves is often presented in two dimensions, and written in terms of the stream function, $\psi(x, z, t)$. In the long-wave limit, relevant to ISWs and KdV-type weakly nonlinear

theories, one expands as

$$\psi = \sum_{n=1}^{\infty} A_n(x,t)\phi_n(z),$$

where ϕ_n are taken as solutions of the eigenvalue problem

$$\frac{d^2\phi}{dz^2} + \frac{N^2(z)}{c^2}\phi = 0 \quad \text{and} \quad \phi(0) = \phi(L_z) = 0,$$

with the propagation speed c being the eigenvalue, and $N^2(z) = \frac{-g}{\rho_0}\frac{\partial \rho}{\partial z}$ is the square of the buoyancy frequency. For a general stratification this eigenvalue problem must be solved numerically (though this is a simple procedure). However, for the case of $N^2(z) = N_0^2 =$ constant, the so-called linearly stratified case, an exact solution can be used to provide insight. For this case

$$\phi_n(z) = \sin\left(\frac{n\pi z}{L_z}\right).$$

This means that for the nth mode the wave-induced horizontal velocity profile is given by

$$u_n(x,z,t) = \frac{n\pi}{L_z}A_n(x,t)\cos\left(\frac{n\pi z}{L_z}\right).$$

Even modes have a wave-induced horizontal velocity maximum at the mid-depth, while odd modes do not. Moreover, for odd modes wave-induced horizontal velocities at the top of the domain are out of phase with wave-induced horizontal velocities at the bottom of the domain, while for even modes the two are in phase. These observations generalize to a generic stratification, even though the analytical form of the wave-induced horizontal velocity profile does not. Indeed for stratification dominated by a sharp pycnocline, it is enough to consider velocities on either side of the pycnocline.

Given that, in both experiments and the coastal ocean, mode-1 and mode-2 waves dominate the other modes from an energetics point of view, a simple criterion for determining the mode of an internal solitary wave is to compare the velocity above and below the pycnocline. A wave is a first (second) mode ISW when the signs of the velocities are opposite (the same). While formally higher mode waves break this description, they are not present to a significant degree in either our simulations or experiments. The explicit form of the mode diagnostic is

$$\frac{u_+ u_-}{c_{\text{in}}^2}, \tag{2}$$

where $u_\pm = u(z = L_z/2 \pm 0.04)$, and the separation choice of 0.04 m was found to give the best contrast in the two wave modes.

During the shoaling process, the incident mode-2 ISW may modify in form because of the changing layer depths. Deepwell *et al.* [13] and Terletska *et al.* [12] characterized the type of interaction by the blocking parameter

$$\frac{a_{\text{in}}}{\ell} = \frac{a_{\text{in}}}{L_z/2 - d - A},$$

where ℓ is the minimum lower layer depth and a_{in} is the incident wave amplitude. When $a_{\text{in}}/\ell > 1$, the lower isopycnal will directly intersect the crest of the ridge, requiring that some form of adjustment must occur. However, significant readjustment is often found before this critical value is reached [12,13].

III. RESULTS: BULK WAVE PARAMETER CHARACTERIZATION

Before discussing the behavior of the waves during and following the interaction with the ridge, we will discuss the mode-2 ISW properties. The amplitude and wavelength (defined as in Deepwell

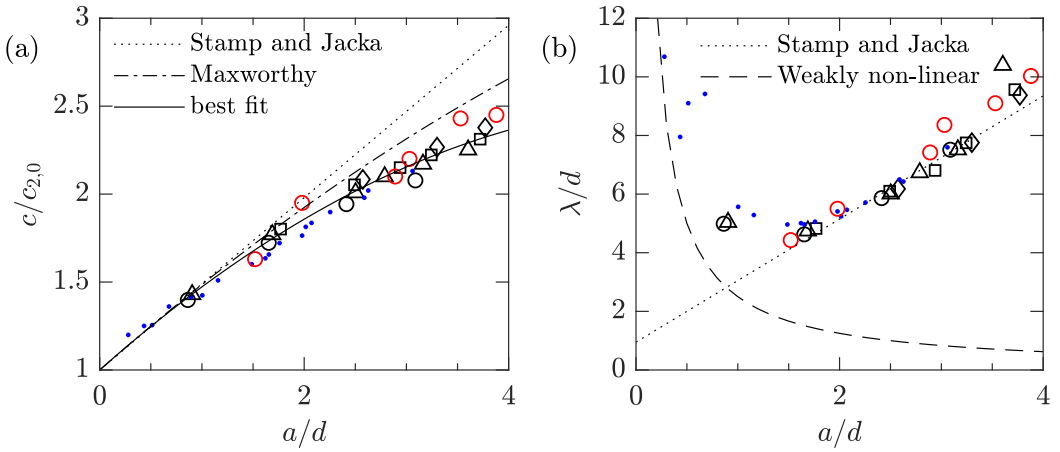

FIG. 2. Mode-2 (a) wave speed versus amplitude and (b) wavelength versus amplitude. Black symbols correspond to incident wave parameters for numerical simulations with L_z depths of (◯) 25 cm, (△) 30 cm, (□) 35 cm, (◇) 40 cm. Red circles are incident experimental data and blue dots are transmitted numerical data.

et al. [13]) were measured at a distance 1.5 m ahead of and behind the peak of the ridge, while the speed was taken to be the average speed over the time period between when the wave settled into a pseudo-steady-state and when it was 1 m ahead of the ridge peak.

As seen previously [6,7,10,30], the speed [Fig. 2(a)] increases with amplitude. We have included the best fits from Stamp and Jacka [6] and Maxworthy [30], even though they both overestimate the speed. A quadratic best fit gives the relationship

$$\frac{c}{c_{2,0}} = 1 + 0.52\frac{a}{d} - 0.044\left(\frac{a}{d}\right)^2, \tag{3}$$

which has a stronger quadratic component than previously seen. It is probable that the differences are caused by the shallow fluid depths relative to the very large wave amplitudes. This causes a limitation on the wave amplitude (and thus the speed) by constraining the wave in shallow depths. Evidence for this is seen by greater speeds and wave amplitudes in a deeper fluid compared to shallower depths with equivalent mixed depths (see Table II for cases with equivalent H_m and different L_z).

The wavelength [Fig. 2(b)] grows with amplitude in the nonlinear regime ($a_{\text{in}}/d \gtrapprox 1.5$), matching the relationship seen in Stamp and Jacka [6],

$$\frac{\lambda}{d} = 0.95 + 2.1\frac{a}{d}.$$

In the small amplitude or weakly nonlinear regime, the wavelength begins to follow the predicted curve (dashed line) from Benjamin [27],

$$\frac{\lambda}{d} = \frac{5d}{2a}.$$

Thus, both the incident and transmitted waves are well described by current theories. We will now shift attention from the incident and transmitted mode-2 ISW onto the generation of other wave types from the interaction of the wave with a broad ridge.

IV. RESULTS: FAR FIELD

The nature of the isolated ridge allows for the analysis of the readjustment of the transmitted wave beyond the topography. Of primary interest is the transfer of energy from the incident mode-2

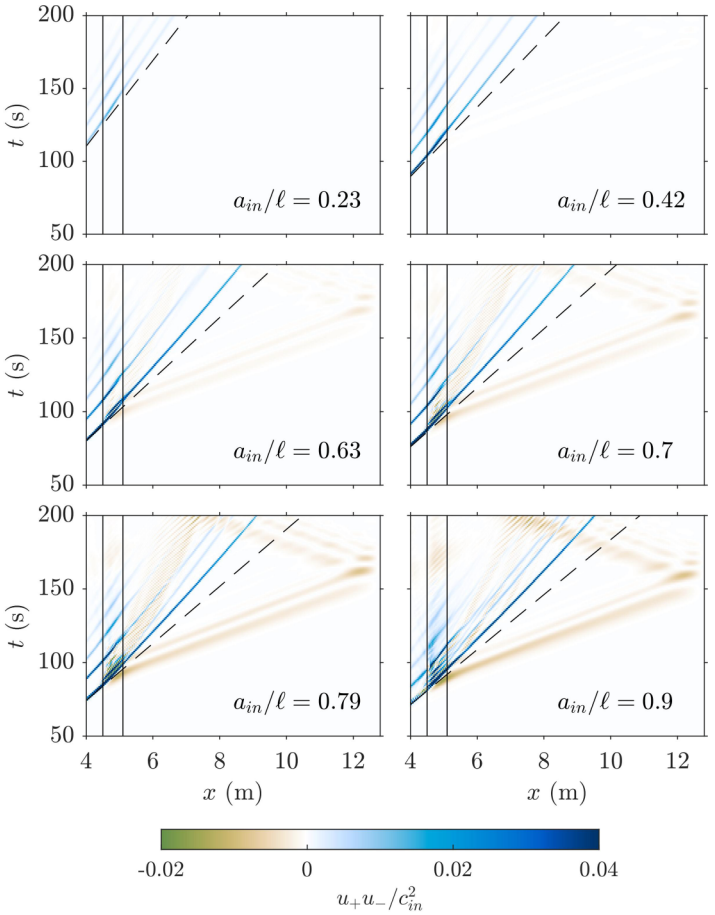

FIG. 3. Internal wave mode diagnostic, u_+u_-/c_{in}^2, for series with a depth of 0.30 m. Vertical lines represent the edges of the ridge. A first (second) mode ISW is represented by brown (blue) coloring. Dashed lines represent the location of the wave if no ridge had been present.

ISW into other waveforms, especially mode 1. Here, we define near field and far field to correspond to the region above and well past (in the direction of wave propagation) the ridge, respectively. Since the laboratory experiments provide detailed information only in the near field, we use the numerical simulations to evaluate the far field.

A. Resultant waves from the wave-ridge interaction

A variety of simulations with different fluid depths were performed; we will use those with a depth of 0.30 m to discuss the wave-ridge interaction in detail because this set of numerical experiments contains the most simulations.

Figure 3 shows the space-time plot of the mode diagnostic, Eq. (2), for the internal wave field during and after the wave-ridge interaction (that is, in the near field and the far field). These illustrate the variety of resultant waves from the wave-ridge interaction. The blocking parameter a_{in}/ℓ is shown for each case, but since ℓ is unchanged within this series it is the amplitude which is the primary controlling factor.

It is evident that there is a connection between wave amplitude (or blocking number) and the resultant wave field. The incident waves are unperturbed by the ridge at low blocking number,

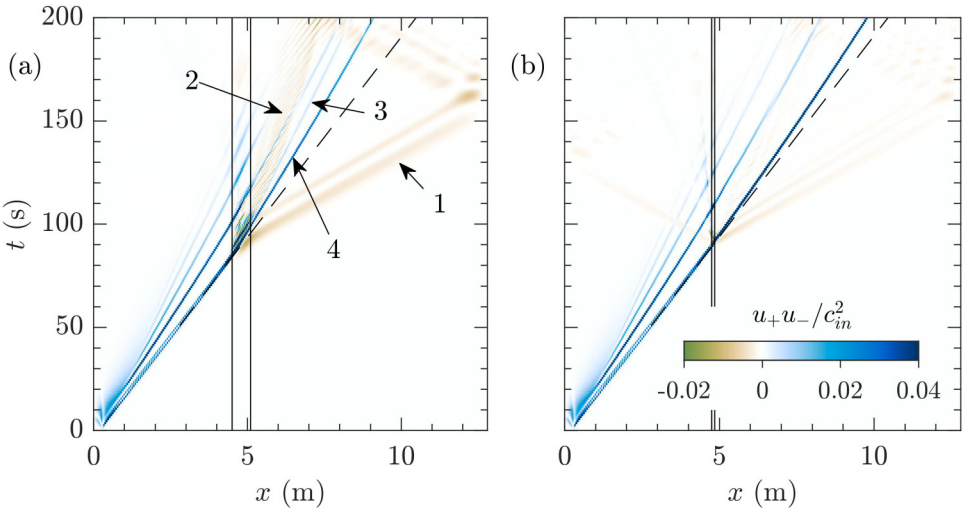

FIG. 4. Internal wave mode diagnostic for case 3010 with (a) $\sigma = 0.60$ m and (b) $\sigma = 0.10$ m. The labels in (a) are (1) leading mode-1 waves, (2) mode-1 dispersive wave train, (3) trailing mode-2 ISW from fissioning of incident wave, and (4) reduced speed of the incident mode-2 ISW. Dashed lines are the same as in Fig. 3.

whereas the wave field becomes busier with increasing blocking number, as seen by the formation of multiple internal waves during the shoaling process.

Three wave types are generated in the most energetic wave-ridge interaction. They are (1) a series of leading mode-1 internal waves, (2) a trailing dispersive wave train (DWT), and (3) a trailing mode-2 ISW. A fourth feature, the deceleration of the incident wave, is also of interest to the shoaling process. Figure 4 shows the wave field for case 3010 for a broad ($\sigma = 0.6$ m) and narrow topography ($\sigma = 0.1$ m). The broad topography case will be used to describe each of the resultant waves in greater detail.

The first feature, the leading mode-1 ISWs, consists of a leading wave of elevation followed by a wave of depression of approximately equal amplitude [brown bands in Fig. 4(a)]. Trailing each of these is another mode-1 wave of elevation with amplitude approximately a quarter of the other two. For case 3010, these waves travel together at wave speed of 0.12 m/s, which is comparable to the long-wave speed of mode-1 ISWs for the given stratification (0.13 m/s). Because of their greater speed, the waves reflect off the end of the channel and return to interfere with the other transmitted waves at a later time.

Trailing behind the initial mode-2 ISW is the second feature, a mode-1 internal wave packet that we have termed a dispersive wave train (DWT). The wave packet in case 3010 contains approximately seven individual waves, though this number increases with blocking parameter. The envelope of the DWT is difficult to quantify due to interference with secondary mode-2 ISWs formed during the initial lock release and because no well-defined envelope exists over the duration of the simulation. The individual waves of the wave packet never exceed the amplitude of the generated leading mode-1 ISWs.

In comparison with Terletska *et al.* [12], who saw the formation of the internal wave packet at all low blocking numbers (or high blocking number using the definition of Terletska *et al.* [12]), we see no such wave formation. This difference is not surprising since the wave traveled onto a step in Terletska *et al.* [12], whereby the fluid depth and thus the properties of the wave guide were permanently altered. In KdV theory this is equivalent to changing the coefficients of the nonlinear and dispersive terms. When the wave travels over a ridge, the change in fluid depth is temporary and the incident wave is only perturbed. This then leads to the question,"How broad does the topography need to be such that the wave packet forms?" As this was not the original motivation for this study

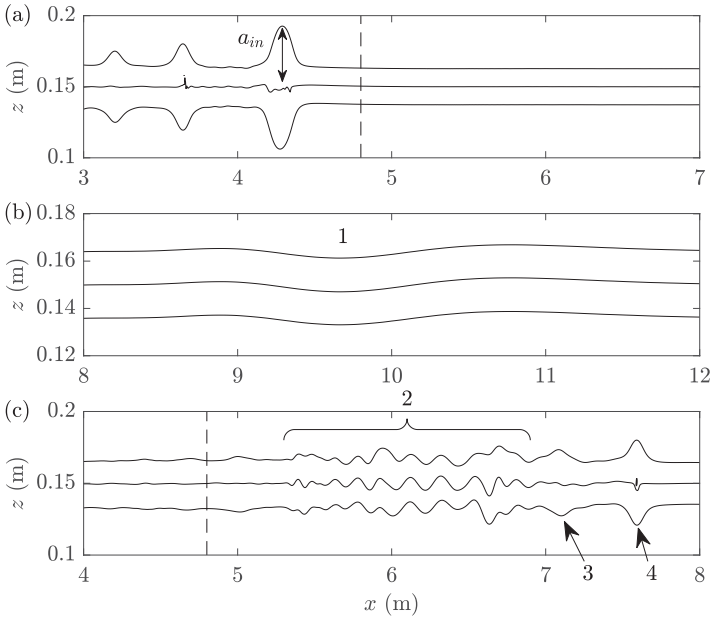

FIG. 5. Isopycnals of the incident and transmitted waves for case 3010. (a) Incident mode-2 ISW at $t = 80$ s, (b) transmitted mode-1 ISWs at $t = 140$ s (1), and (c) dispersive wave train (2), mode-2 ISW from fissioning (3), and transmitted mode-2 ISW (4) at $t = 160$ s. Location of the ridge crest is denoted by a vertical dashed line. Note the change in vertical and horizontal scales in (b) to accentuate the leading, small amplitude mode-1 waves.

(i.e., the physical experiments were not designed with this question in mind) we will leave it for future investigation.

The third feature, the trailing mode-2 ISW, is a result of the splitting of the incident mode-2 ISW into two transmitted mode-2 ISWs. This process is novel from an experimental perspective as it has yet to be documented for shoaling mode-2 ISWs, though it can be predicted qualitatively with KdV theory [31]. More quantitative comparisons between experiment and simulation are better carried out with a numerical model of the full stratified Navier-Stokes equations, since Lamb and Xiao [23] have shown that a broad range of WNL theories make some phase and amplitude errors during the shoaling process. Other processes, such as the mixing of the pycnocline [19], have led to the generation of trailing mode-2 ISWs in strong interactions. The mechanism here is not mixing but rather a temporary delay of the lower region of the incident mode-2 ISW which becomes the secondary wave, though mixing may play a secondary role. In the deepest cases ($L_z = 40$ cm) the fissioned mode-2 ISW was very difficult to observe since the internal wave packet dominated the trailing wave field.

Lastly, as a result of the fissioning, the incident mode-2 ISW experiences a reduction in wave speed because of the reduction in wave amplitude [compare sizes in Figs. 5(a) and 5(c)]. The transmitted wave speed was found to be 20% slower than the incident wave speed.

Though weaker than the leading mode-1 ISWs (by about a fifth in wave amplitude), reflected waves of both mode 1 and mode 2 were observed. Revisiting the narrow topography cases of Deepwell *et al.* [13] [Fig. 4(b)] shows the reflected waves to be considerably larger when shoaling over a narrow ridge. For this particular comparison, the reflected waves are so small in the broad case that they are not evident in the figure. Though the wave generation was not the focus of that study, a reflected mode-1 ISW was created in the narrow topography version of cases 3010 and 3012. Case 3012 also saw the formation of a reflected mode-2 wave (not presented). This discrepancy in the

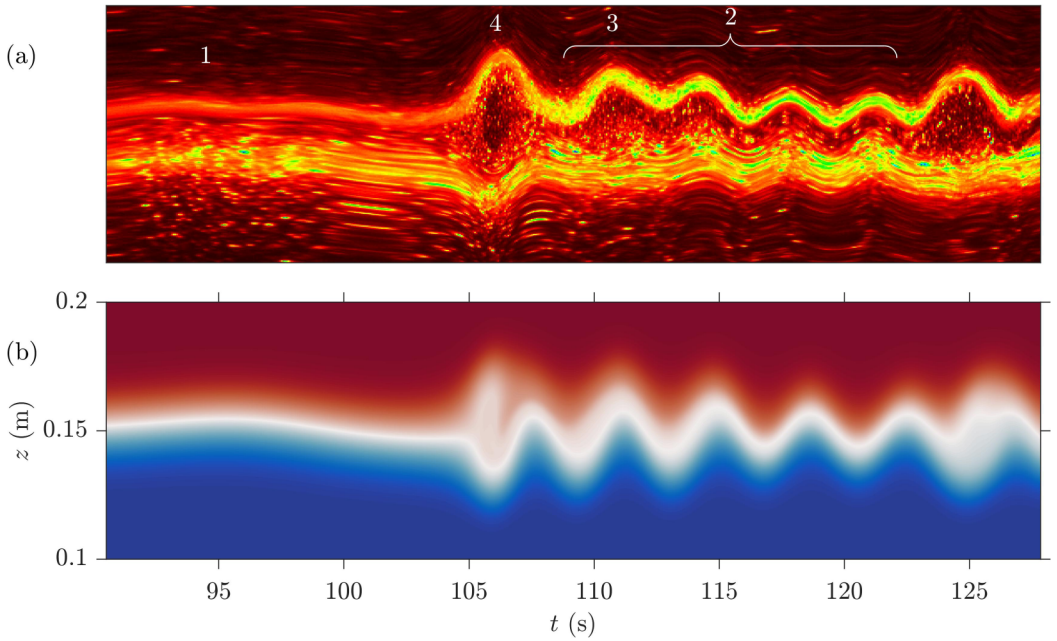

FIG. 6. Density time series at $x = 5.4$ m for (a) experimental case 3010e and (b) numerical case 3010.

reflected waves is explained by the abruptness of the narrow topography compared to the currently analyzed broad case. Quantitatively, this is better seen with the Iribarren number, $\mathrm{Ir} = s_{\max}/\sqrt{a/\lambda}$, where $s_{\max}$ is the maximum slope and λ is the wavelength. Ir has values of 1.3 and 0.2 for the narrow and broad cases, respectively, though we may be stretching the applicability of this metric as it was designed for waves shoaling *on* a slope rather than *over* a ridge. In strong interactions with a narrow topography, the extraction of the core fluid [look ahead to Fig. 10(a)] creates both (1) mode-1 ISWs through the deflection of the pycnocline while the extracted fluid returns to its equilibrium depth, and (2) mode-2 ISWs by the mixing of the pycnocline. The reflected waves are weak, with amplitudes approximately those of the leading transmitted mode-1 waves.

Figure 5 shows instantaneous density fields for the (a) incident and (b,c) transmitted waves. Note the change in vertical scale for Fig. 5(b) compared to the other panels to accentuate the small amplitudes of the leading mode-1 ISWs. The dispersive wave train has no easily described envelope, but is similar in amplitude to the trailing mode-2 ISW.

The spatial region recorded in the experiments is not as large as that of the numerical simulations, which makes measuring the long-term impacts of the wave-ridge interaction more difficult. However, the time series of the resultant wave field at $x = 5.4$ m shows behavior similar to the simulations (Fig. 6). There is clear evidence of (1) the leading mode-1 ISW, (2) the trailing dispersive wave train, and (4) the transmitted mode-2 ISW. The trailing mode-2 wave (3) is difficult to observe at this location because of the interference with the trailing mode-1 wave packet. Regardless, the predicted time at which this wave passes through this plane is shown based on the velocity and position from a later time. Near the end of this time series, at approximately $t = 125$ s, a trailing mode-2 ISW generated from the initial density collapse enters the viewing region.

B. Factors in wave-ridge interaction strength

The majority of articles on shoaling ISWs have used the blocking parameter a_{in}/ℓ, or something similar, as an indicator of the interaction type. However, though we have used this value thus far, we find that it is not sufficient in categorizing the wave-ridge interaction when fluid depth

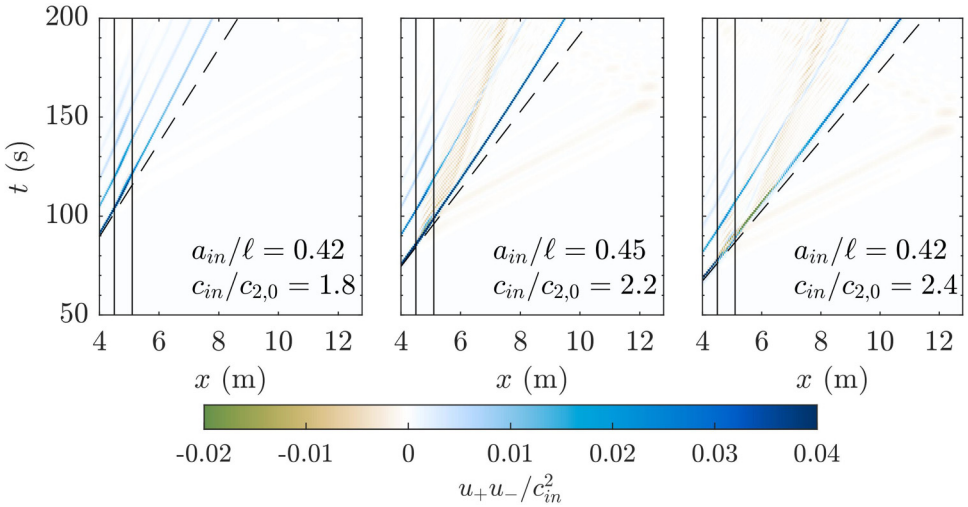

FIG. 7. Internal wave mode diagnostic for cases 3006 (left), 3509 (center), and 4012 (right). Dashed lines are the same as in Fig. 3.

is varied. Three cases with similar blocking parameters, but with different depths L_z and initial wave amplitudes a_{in} experienced different wave-ridge interactions (Fig. 7). Case 3006 experienced minimal adjustment of the incident mode-2 ISW while cases 3509 and 4012 clearly formed a DWT even though they all had the same blocking parameter.

A second factor, the wave speed, also affects the strength of the interaction. Based on an impulse-type argument, where a wave of greater initial energy experiences a greater change in momentum, a difference in wave formation may arise at different incident speeds. This is made clear by comparing the wave speeds for each case with similar blocking parameter (Fig. 7). In the case of a shoaling mode-1 ISW, Sveen *et al.* [19] used a lower layer velocity criterion to demarcate breaking regimes. Rather than looking at the lower layer velocity, we use the incident wave speed since the two should be proportional.

C. Quantitative characterizations of the resultant waves

The previous section provided a clear overview of the resultant wave field, specifically that new internal waves are generated to a degree that depends on the incident amplitude and speed. Specifically, there is the issue that the blocking parameter used in Terletska *et al.* [12], a_{in}/ℓ, is not sufficient to classify and characterize the resultant waves. In this section, we quantify resultant wave parameters as a function of the incident wave and fluid depth.

The amplitude a and speed c of the incident, transmitted, and generated mode-1 and mode-2 internal waves are presented in Fig. 8. The DWT was not well represented by any wave envelope and was therefore impossible to characterize. We denote the incident and transmitted mode-2 ISWs with subscripts in and tr, respectively, while the generated waves are denoted by their mode number. We will now discuss the results of each resultant wave individually before discussing them all as a whole.

The wave speed of the generated, leading mode-1 ISW, c_1, is found to be independent of all incident wave parameters. Rather, the speed is approximately proportional to the mode-1, linear, long-wave speed for a stratification consisting of two layers of equal depth:

$$c_{1,0} = \sqrt{\frac{g\Delta\rho}{\rho_0}\frac{L_z}{4}}.$$

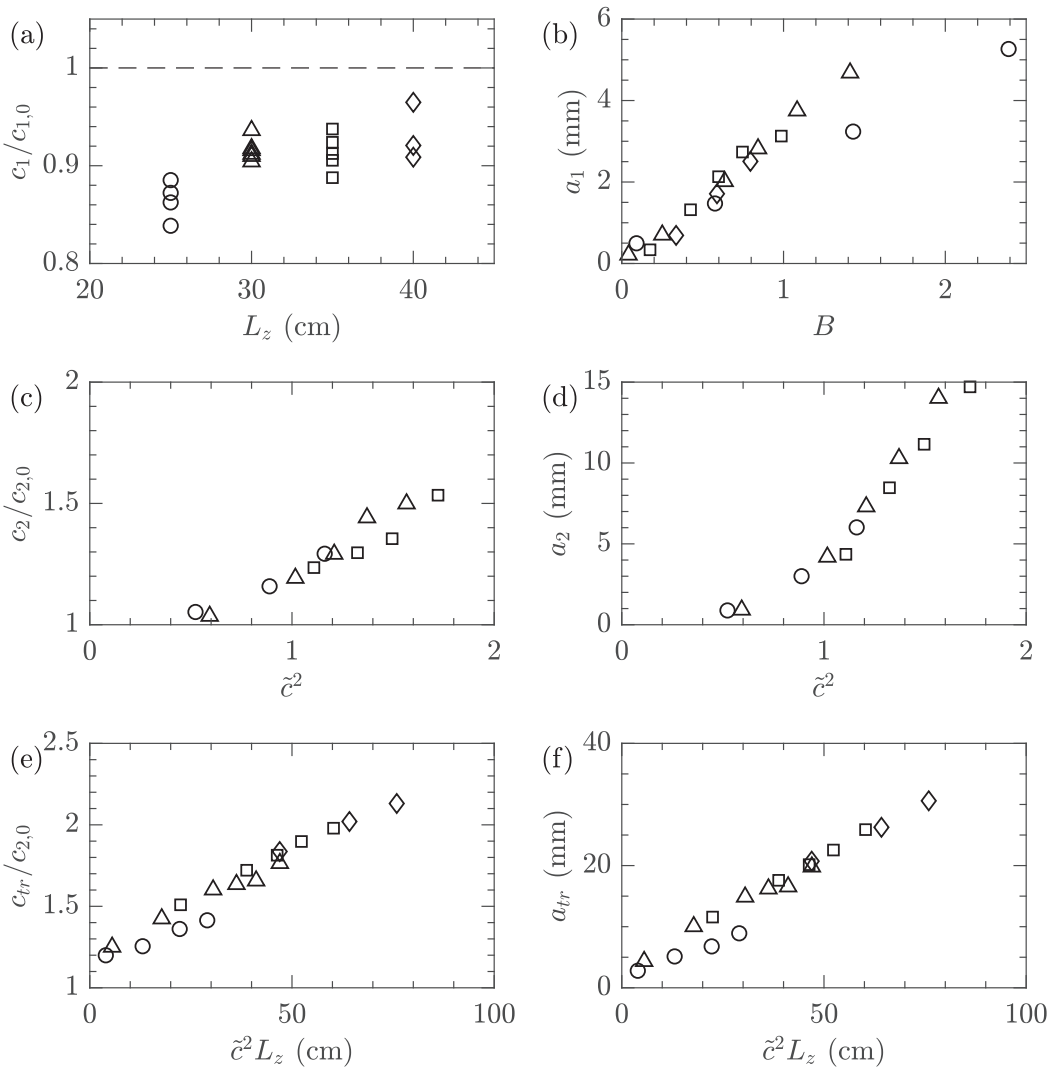

FIG. 8. Wave speed (first column) and amplitude (second column) of the (a,b) mode-1 wave, (c,d) trailing mode-2 wave, and (e,f) transmitted mode-2 wave. Symbols correspond to $L_z$depths (◯) 25 cm, (△) 30 cm, (□) 35 cm, (◇) 40 cm. The dashed line in (a) is the expected mode-1, long-wave speed.

This is consistent with ISWs of small amplitude which travel at speeds completely independent of the generation mechanism. The only discrepancy is that, on average, the measured speed is 10% slower than that of the predicted speed [dashed line in Fig. 8(b)]. This difference is accounted for by the relatively short wavelengths of the wave, $\mathcal{O}(1\text{ m})$, where the long-wave limit is inapplicable. Variations in the wavelength are also responsible for the different speeds at each fluid depth L_z.

Unlike the speed, the amplitude of the leading mode-1 ISW is dependent on the strength of the wave-ridge interaction. A stronger blocking by the ridge will deflect the incident wave upwards, which breaks the symmetry across the pycnocline center, allowing for mode-1 ISWs to form. Therefore, a correlation exists between the blocking and the mode-1 ISW wave amplitude. As in the previous section, the blocking parameter a/ℓ from Terletska *et al.* [12] and Deepwell *et al.* [13] does not correctly account for the resultant wave amplitude for all fluid depths. Instead, the modified

blocking parameter,

$$B = \frac{a_{\text{in}}}{\ell}\tilde{c}^2, \tag{4}$$

where

$$\tilde{c} = \frac{c_{\text{in}}}{c_{2,0}} - 1,$$

is a clear predictor of the mode-1 ISW wave amplitude Fig. 8(b)]. Equation (4) extends the blocking parameter from Terletska *et al.* [12] and Deepwell *et al.* [13] to also include the incident wave speed. In fact, B depends on the square of the speed, indicating that the incident kinetic energy is important for the interaction, in addition to the percentage of wave blocking (a_{in}/ℓ).

Alternatively, B can be recast into a wave amplitude form using Eq. (3), which converts speed into an amplitude. At low amplitude the quadratic term may be ignored, giving

$$B \approx 0.27\frac{a_{\text{in}}^3}{\ell d^2}.$$

Thus, there is an equivalent definition which primarily depends on the amplitude. The prior definition is more intuitive since it is not clear how the pycnocline thickness d should affect the wave-ridge interaction.

We note that the modified blocking parameter B is only valid when the peak of the ridge is below the pycnocline. In a case where the peak of the ridge were to intersect the pycnocline, B would become unbounded. The linear relationship between the mode-1 amplitude and B [Fig. 8(b)] would thus imply that the amplitude of the leading mode-1 wave would also approach infinity, which is clearly unphysical. This impact is already apparent for cases 2508 and 2510 [two circles on right of Fig. 8(b)] which have the large wave amplitudes in shallow depths. In such a situation, greater wave reflection would be expected and a separate theory would need to be presented. Since ocean ridges generally do not intercept the pycnocline, we suggest that our results are valid for such cases.

As far as we are aware this is the first experimental indication of a shoaling mode-2 ISW fissioning into two separate mode-2 ISWs (though it is qualitatively predicted by KdV theory). Not unlike the splitting of atomic particles, this process requires sufficient initial energy for the fissioning process to occur. The square of the modified incident wave speed, $\tilde{c}^2$, is a suitable choice and shows that the amplitude and wave speed of the trailing mode-2 ISW grows with incident pseudo-kinetic-energy (second row of Fig. 8). A transition point occurs at $\tilde{c}^2 = 1/2$. For $\tilde{c}^2 > 1/2$ the amplitude of the trailing mode-2 wave grows linearly with increasing kinetic energy. When $\tilde{c}^2 < 1/2$ the amplitude is small compared to the pycnocline width ($a_2/d \lessapprox 0.3$) and the waves are difficult to observe.

The speed of the trailing, fissioned mode-2 ISW at the smallest pseudo-kinetic-energy is well approximated by the expected mode-2 speed [Eq. (1)]. The wave speed increases with pseudo-kinetic-energy because the amplitude is similarly correlated and thus the speed grows with amplitude. Cases with a depth of 40 cm had evidence of fissioned mode-2 waves but these were drastically impacted by the coincident DWT and have therefore been removed from detailed consideration. However, this indicates that the fissioning occurs primarily at depths intermediate between deep layers, where the incident wave is only marginally impacted by the hill, and very shallow layers, where the incident wave experiences greater reflection than transmission at the hill. As the fissioning of the mode-2 ISW appears to be novel, it would be encouraging to observe such an event in nature. This, however, might be difficult since nature is far more chaotic due to the presence of background shear [17], other internal waves, and a stratification which is not ideal for mode-2 ISWs [11,25].

Lastly, the transmitted mode-2 ISW is dependent on a separate set of parameters than that of the previous waves, namely the product of the incident pseudo-kinetic-energy and the fluid depth, $\tilde{c}^2 L_z$ [Figs. 8(e) and 8(f)]. This contradicts results of Terletska *et al.* [12] which required a blocking parameter such as that used to explain the mode-1 wave amplitude. One such explanation for this

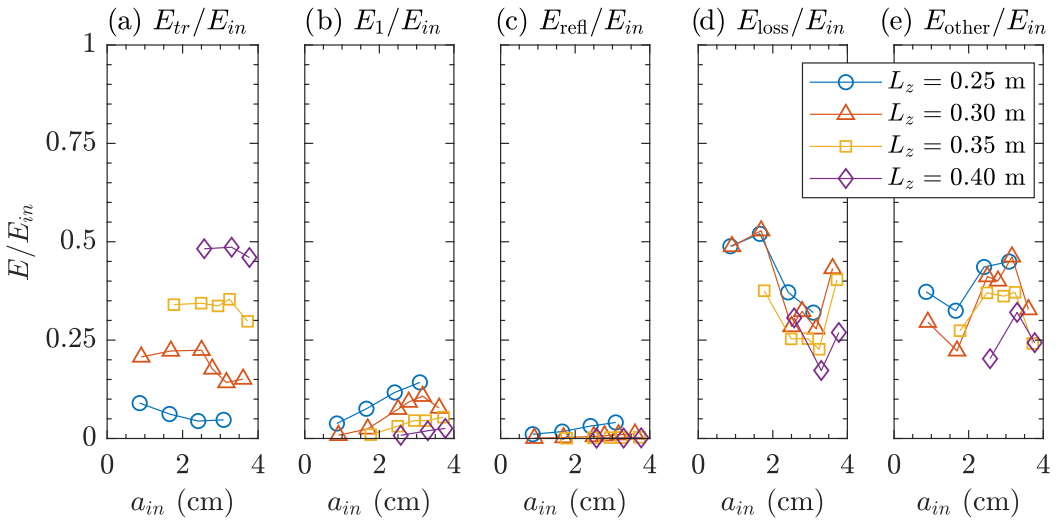

FIG. 9. Energy of the resultant waves. (a) Transmitted mode-2 ISW, (b) leading mode-1 wave, (c) reflected mode-1 wave, (d) predicted energy loss between the measurement locations before and after the hill if the topography was not present, and (e) all other energy components (fissioned mode-2 wave, dispersive wave train, and dissipation due to mixing caused by the wave-hill interaction).

discrepancy is that, here, the incident wave is capable of reforming since the change in topography is only temporary.

D. Energy of the resultant waves

Following the work of Lamb and Nguyen [32], the pseudoenergy equation for a fluid without diffusivity and viscosity is

$$\frac{\partial}{\partial t}(E_k + E_a) + \nabla \cdot [\vec{u}(E_k + E_a + p_d)] = 0, \tag{5}$$

where E_k is the kinetic energy density, E_a is the available potential energy, p_d is the pressure perturbation due to waves, and $E_k + E_a$ is the pseudoenergy density.

From (5) it is clear that over a fixed volume enclosing the fluid depth, the energy fluxes through the lateral boundaries are

$$K_f = \int_{h(x)}^{L_z} uE_k \, dz, \tag{6}$$

$$\text{APE}_f = \int_{h(x)}^{L_z} uE_a \, dz, \tag{7}$$

$$W = \int_{h(x)}^{L_z} up_d \, dz, \tag{8}$$

where K_f, APE_f, and W are the kinetic energy and available potential energy fluxes and the work done by the pressure perturbation associated with the waves, respectively. From this, the total pseudoenergy within a wave is

$$E = \int_{t_1}^{t_2} K_f + \text{APE}_f + W \, dt, \tag{9}$$

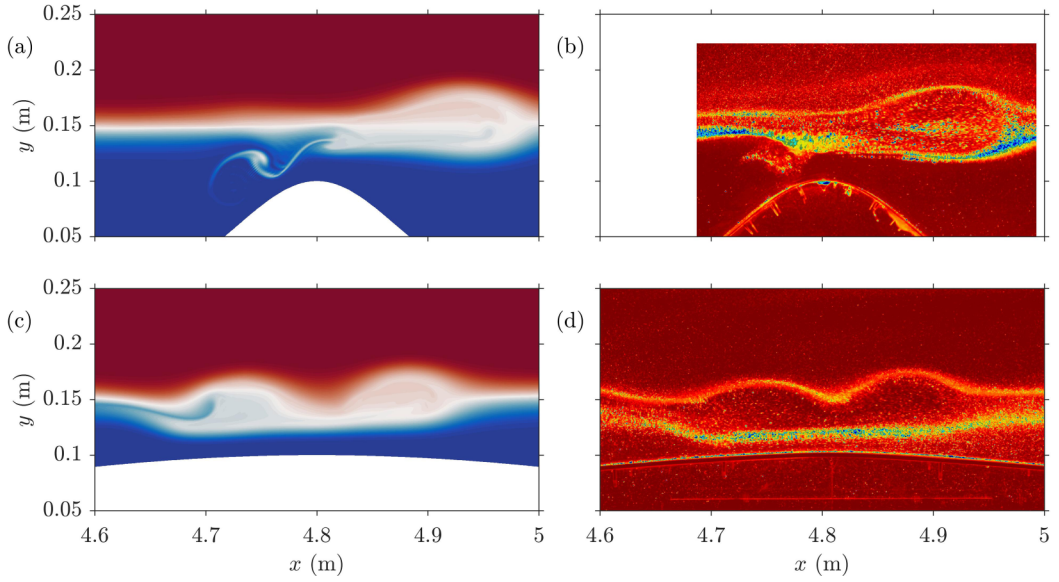

FIG. 10. Density field from numerical simulations (left column) and experimental false color image (right column) of a mode-2 ISW passing over the ridge at $t = 93$ s for case 3010 with a ridge width of (a,b) 0.10 m (data courtesy of Deepwell *et al.* [13]) and (c,d) 0.60 m.

where $[t_1, t_2]$ is an appropriate time interval for the passage of the wave through the plane $x = x_r$, where x_r is an appropriate position.

The incident and reflected pseudoenergy was calculated at $x = x_0 - 2$, while the transmitted pseudoenergy was calculated at $x = x_0 + 2$ (either 2 m before or after the crest of the hill). Since the lock-release mechanism formed a series of incident waves, many of which interact with the waves formed from the wave-hill interaction, we have rerun all simulations having removed the initial secondary waves. This greatly simplified the analysis of the generated waves.

Figure 9 presents these results when scaled by the incident pseudoenergy (E_{in}). The transmitted mode-2 wave energy E_{tr} [Fig. 9(a)] is seen to increase with fluid depth from about 5–10% of the initial pseudoenergy at $L_z = 0.25$ m to approximately 50% at $L_z = 0.40$ m, indicating that the strongest wave-hill interaction occurs in the shallowest cases when the pycnocline is close to the topography.

Figure 9(b) further emphasizes this since the leading mode-1 ISW grows in energy with decreasing fluid depth. At its peak, the leading mode-1 ISW contains approximately 14% of the initial pseudoenergy for case 2510. Furthermore, the reflected waves were largest in the shallowest cases [Fig. 9(c)], though their contribution to the overall budget is fairly insignificant; no reflected wave contained greater than 5% of the incident energy.

The incident mode-2 wave was lossy, as both the incident energy and wave amplitude would decrease with time before interacting with the ridge. To account for this dissipation, the energy passing through the planes $x = x_0 - 2$ and $x = x_0 - 1.5$ was compared to find an average loss of energy over distance. Extrapolating this to $x = x_0 + 2$ gives the expected loss of energy without topography [Fig. 9(d)]. The dissipation values can be considerable (up to 50%), and we suspect that they are caused by the relatively high diffusivity compared to the physical value (though we do reasonably well for numerical simulations in this regard).

Difficulties arise in decomposing the energy between the fissioned mode-2 wave and the dispersive wave train since both travel through the measurement plane nearly simultaneously. Furthermore, a direct measurement requires significant time, which results in the leading mode-1 ISW interfering with these waves after reflecting off the end wall. Therefore, the energy within

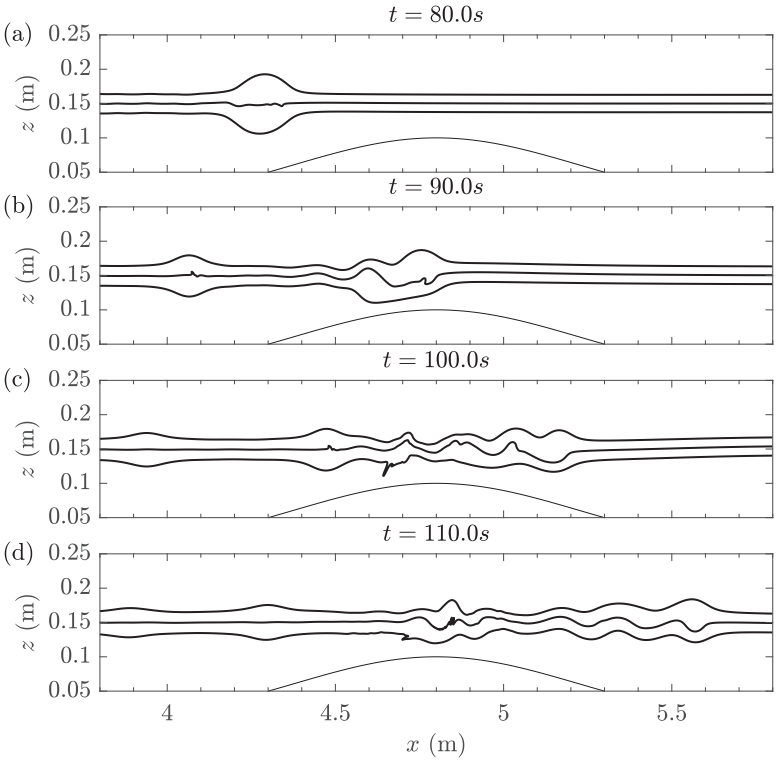

FIG. 11. Time series of isopycnals for case 3010.

the fissioned mode-2 wave, the DWT, and the energy lost due to mixing caused by the wave-hill interaction are indirectly measured as the remainder of the energy budget [Fig. 9(e)]. The energy in these components is comparable to that lost due to diffusion and to the transmitted mode-2 energy, and in the shallowest cases is significantly larger than the transmitted mode-2 energy.

V. RESULTS: NEAR FIELD

A. Wave adjustment

As this article is a direct comparison to Deepwell *et al.* [13], but with broader topography, we will now contrast two cases with matching incident wave conditions. Figure 10 illustrates clearly the fundamental differences between the narrow and broad cases.

There are two main differences in the observed ISW behavior over the topography. First, the narrow case displays the filamentary extraction of wave core material, while the ISW in the broad case has separated into two mode-2 ISWs. Furthermore, the leading mode-2 ISW in the broad ridge case has decelerated and lags behind the mode-2 ISW in the narrow case.

Both of these changes are a result of a greater removal of wave core fluid from the incident ISW in the broad case. Since the topography is wide compared to the wavelength of the approaching ISW, the entire ISW spends a significant amount of time over the broad ridge as compared to the narrow ridge (approximately six times longer in the broad case).

Figure 11 shows the evolution of the incident mode-2 ISW for case 3010 over broad topography. The incident wave is stable when it reaches the ridge where the lower portion of the wave becomes obstructed, which causes it to lag behind the upper portion [notice the horizontal location of the maximum displacement of the lower isopycnal in Fig. 11(b) and the downward deflection of the

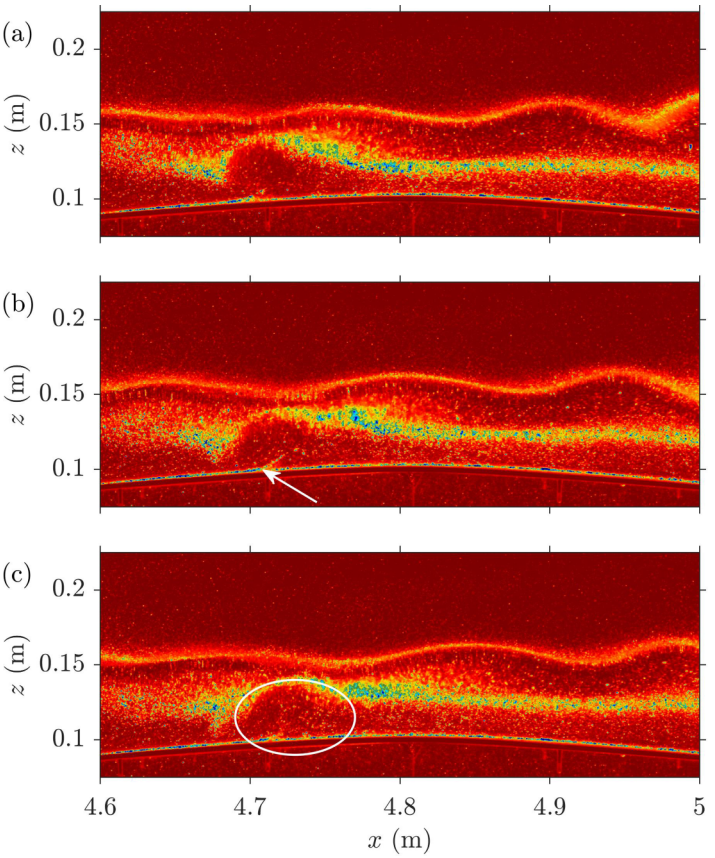

FIG. 12. False color time series of the raw image for case 3010e: (a) 5.4 s, (b) 6.4 s, and (c) 7.4 s after the wave passed directly over the peak. The arrow in (b) points to the separation point and the ellipse in (c) highlights the region of resuspended material.

middle isopycnal into the lower portion of the wave]. The obstruction has also created a series of trailing mode-1 waves [Fig. 11(d)]. The formation of these waves can also be partially explained by a shear layer where the wave-induced velocities become significantly asymmetrical with respect to the pycnocline center [17]. The transmitted wave amplitude is also noticeably smaller than the incident wave.

B. Boundary layer separation

Deepwell *et al.* [13] observed a resuspension of bottom boundary layer material in moderate and strong wave-ridge interactions due to strong vortex formation near the peak of the ridge. With broad topography, resuspension was only seen in case 3010e. This case has a shallow fluid depth and large wave amplitude and is thus similar to the cases with resuspension using a narrow ridge.

Figure 12 (case 3010e) shows a few snapshots of the resuspension. There is a clear separation point that forms in the high vortex region, which has caused particles lying on the bottom boundary to be resuspended [Fig. 12(b)]. Though the parameters of the particles (such as particle size and density) play a role in resuspension, we highlight the formation of the separation point and the possibility for resuspension to occur coincident with the separation. A second later, the vortex has disintegrated into a chaotic region (encircled).

The Reynolds numbers of experiments are generally larger than that of the simulations, and field conditions are at least an order of magnitude higher. The role of increased Reynolds number was

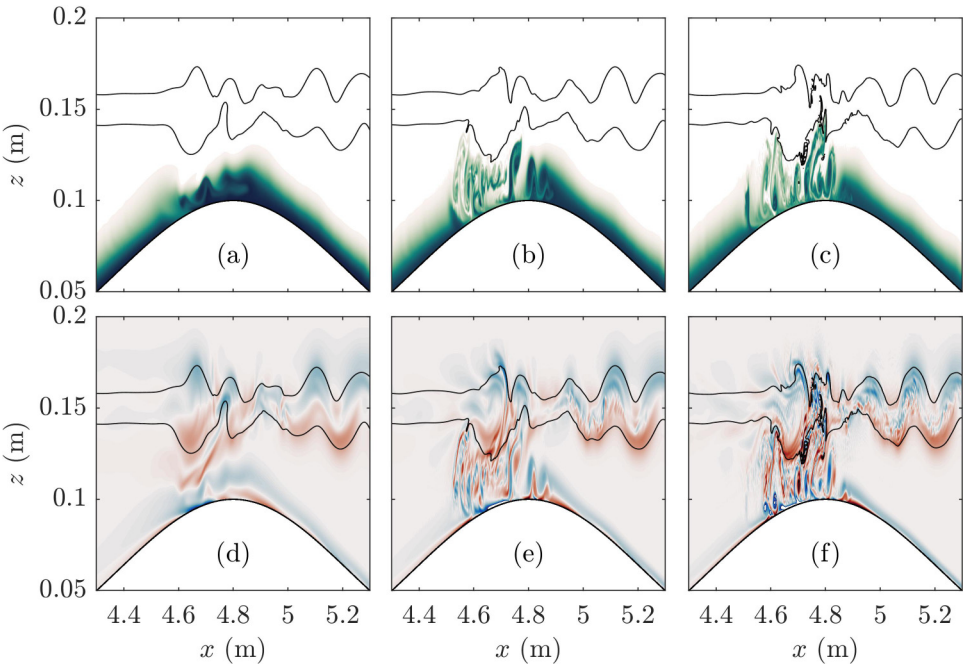

FIG. 13. Bottom tracer (top row) and vorticity (bottom row) for case 3010 with Reynolds number (a,d) unaffected, (b,e) doubled, and (c,f) quadrupled. Snapshots are at $t = 105$ s (14 s after the wave passed directly over the peak). Black contours are isopycnals designating the resultant wave field. Vorticity ranges between -10 and 10 s^{-1}.

explored by running two further simulations with double and quadruple the Reynolds number of the original simulation. These were initialized from the original simulation as the wave neared the hill. To maintain comparison to the previous cases, the viscosity was changed rather than the wave speed or pycnocline thickness. To ensure that any change was purely a result of the Reynolds number, the Schmidt number was held fixed.

Comparison of the bottom tracer field (initialized as a 1 cm thick passive field along the bottom boundary) and vorticity for the different Reynolds numbers is shown in Fig. 13. The tracer field is seen to move higher in the water column with increasing Reynolds number, while the vorticity field becomes increasingly chaotic, with considerably more localized, small-scale features. The overall structure of the wave features in the density field is consistent in all three experiments, but again as the Reynolds number increases more and more small-scale features are apparent.

In Deepwell *et al.* [13] particle resuspension was correlated with wave breaking, of which there is little with a broad topography since the wave fissions rather than breaks. The above results suggest that the type of adjustment observed over broad topography does not produce sufficient boundary layer vorticity to excite resuspension when the Reynolds number is too low. Hence, a broad topography requires a higher Reynolds number for an equivalent wave-ridge interaction to produce any cross-bottom boundary layer transport. Cross boundary layer transport is possible for wide ridges, and is associated with small-scale instability of flow in the curved boundary layer over the crest of the ridge as the largest waves pass over it. This is quite different than for a narrow ridge, in which case resuspension and vortex generation are observed in all strong interaction cases, even at relatively low Reynolds number. As it was not the primary purpose of this study to study the Reynolds number dependance on the vorticity generation, we shall leave further exploration of this for a future study.

VI. SUMMARY

We have investigated the transit of mode-2 ISWs over a broad ridge using both numerical simulations and laboratory experiments. The incident mode-2 wave was found to generate multiple internal waves, and wave types, from the interaction with the ridge at sufficiently high amplitude and wave speed. At most, four wave types resulted from the interaction: leading, small amplitude mode-1 ISWs, a trailing wave packet, a fissioned mode-2 ISW, and the transmitted, but decelerated, mode-2 ISW. The fissioning of a trailing mode-2 ISW from the incident wave is consistent with KdV theory, but to our knowledge was not previously documented in the field or experimentally.

No universal parameter was found to predict the characteristics (the amplitude and wave speed) of all resultant waves. Rather, each resultant wave had a separate condition based on the incident wave velocity, amplitude, and fluid depth.

Broadly speaking, there is some similarity between the results of Terletska *et al.* [12] and those presented here; namely, the generation of the same types of waves during shoaling and transit of the wave was found. However, significant difference exist. The blocking parameter used by Terletska *et al.* [12] was unable to predict the strength of the resultant waves, and different metrics were presented. Furthermore, contrary to Terletska *et al.* [12], at low wave amplitude the waves were unaffected by the passage over the ridge. This indicates that in the linear and weakly nonlinear regimes there is a minimum duration for which the wave must remain over a change in topography to be permanently altered. This is further seen in the comparison between different ridge widths, where greater wave adjustment occurred over the broader ridge. Quantifying the impact of varying ridge width is thus a natural progression of this research.

One such experiment saw weak scouring and resuspension of bottom boundary layer material. Cross boundary layer transport was seen to be correlated with Reynolds number. At higher Reynolds numbers the vorticity near the crest of the ridge became more chaotic, in association with the cross boundary transport.

Future work should consider extensions to more field appropriate conditions. As mentioned earlier, one possibility is to increase the Reynolds number to field scale values, though this would require care as the Chebyshev method leads to a boundary layer clustering that scales with the square of the number of points in the vertical. Thus, maintaining a reasonable time step while resolved both the boundary layer and the main water columns would be challenging. A second avenue worthy of exploration would consider the effects of short-scale undulations superimposed on the broad ridge. Finally, three-dimensional simulations are necessary to properly assess vorticity dynamics and viscous dissipation.

ACKNOWLEDGMENTS

This research was supported by the Natural Sciences and Engineering Research Council of Canada through a Discovery Grant, RGPIN-311844-37157 (M.S.), and the Government of Ontario through a Queen Elizabeth II Graduate Scholarship in Science and Technology (D.D.). The experimental work was conducted at The University of Dundee by D.D. and M.C. with the aid of grants provided by The University of Dundee, the University of St Andrews, and the University of Waterloo. We also acknowledge the skillful technical assistance provided by John Anderson and David Turbyne. The authors would also like to acknowledge the constructive criticism and suggestions given by the two anonymous referees.

[1] M. H. Alford, T. Peacock, J. A. MacKinnon, J. D. Nash, M. C. Buijsman, L. R. Centurioni, S.-Y. Chao, M.-H. Chang, D. M. Farmer, O. B. Fringer, K.-H. Fu, P. C. Gallacher, H. C. Graber, K. R. Helfrich, S. M. Jachec, C. R. Jackson, J. M. Klymak, D. S. Ko, S. Jan, T. M. S. Johnston, S. Legg, I.-H. Lee, R.-C. Lien, M. J. Mercier, J. N. Moum, R. Musgrave, J.-H. Park, A. I. Pickering, R. Pinkel, L. Rainville, S. R. Ramp,

D. L. Rudnick, S. Sarkar, A. Scotti, H. L. Simmons, L. C. St Laurent, S. K. Venayagamoorthy, Y.-H. Wang, J. Wang, Y. J. Yang, T. Paluszkiewicz, and T.-Y. (David) Tang, The formation and fate of internal waves in the South China Sea, Nature (London) **521**, 65 (2015).

[2] S. R. Ramp, Y. J. Yang, D. B. Reeder, and F. L. Bahr, Observations of a mode-2 nonlinear internal wave on the northern Heng-Chun Ridge south of Taiwan, J. Geophys. Res.: Oceans **117** (2012).

[3] S. R. Ramp, Y. J. Yang, D. B. Reeder, M. C. Buijsman, and F. L. Bahr, The evolution of Mode-2 nonlinear internal waves over the northern Heng-Chun ridge south of Taiwan, Nonlinear Processes Geophys. Discuss. **2**, 243 (2015).

[4] J. C. B. da Silva, M. C. Buijsman, and J. M. Magalhaes, Internal waves on the upstream side of a large sill of the Mascarene Ridge: A comprehensive view of their generation mechanisms and evolution, Deep Sea Res. Part I **99**, 87 (2015).

[5] E. L. Shroyer, J. N. Moum, and J. D. Nash, Mode 2 waves on the continental shelf: Ephemeral components of the nonlinear internal wavefield, J. Geophys. Res. **115** (2010).

[6] A. P. Stamp and M. Jacka, Deep-water internal solitaty waves, J. Fluid Mech. **305**, 347 (1995).

[7] M. Salloum, O. M. Knio, and A. Brandt, Numerical simulation of mass transport in internal solitary waves, Phys. Fluids **24**, 16602 (2012).

[8] A. Brandt and K. R. Shipley, Laboratory experiments on mass transport by large amplitude mode-2 internal solitary waves, Phys. Fluids **26**, 46601 (2014).

[9] R. E. Davis and A. Acrivos, Solitary internal waves in deep water, J. Fluid Mech. **29**, 593 (1967).

[10] D. E. Terez and O. M. Knio, Numerical simulations of large-amplitude internal solitary waves, J. Fluid Mech. **362**, 53 (1998).

[11] M. Carr, P. A. Davies, and R. P. Hoebers, Experiments on the structure and stability of mode-2 internal solitary-like waves propagating on an offset pycnocline, Phys. Fluids **27**, 046602 (2015).

[12] K. Terletska, K. T. Jung, T. Talipova, V. Maderich, I. Brovchenko, and R. Grimshaw, Internal breather-like wave generation by the second mode solitary wave interaction with a step, Phys. Fluids **28**, 116602 (2016).

[13] D. Deepwell, M. Stastna, M. Carr, and P. A. Davies, Interaction of a mode-2 internal solitary wave with narrow isolated topography, Phys. Fluids **29**, 076601 (2017).

[14] C. Yuan, R. Grimshaw, and E. Johnson, The evolution of second mode internal solitary waves over variable topography, J. Fluid Mech. **836**, 238 (2018).

[15] M.-H. Cheng, C.-M. Hsieh, J. R. Hsu, and R. R. Hwang, Transformation of mode-2 internal solitary wave over a pseudo slope-shelf, AIP Adv. **7**, 095309 (2017).

[16] C. Guo and X. Chen, Numerical investigation of large amplitude second mode internal solitary waves over a slope-shelf topography, Ocean Model. **42**, 80 (2012).

[17] P. Zhang, Z. Xu, Q. Li, B. Yin, Y. Hou, and A. K. Liu, The evolution of mode-2 internal solitary waves modulated by background shear currents, Nonlinear Processes Geophys. **25**, 441 (2018).

[18] K. G. Lamb, O. Polukhina, T. Talipova, E. Pelinovsky, W. Xiao, and A. Kurkin, Breather generation in fully nonlinear models of a stratified fluid, Phys. Rev. E **75**, 46306 (2007).

[19] J. K. Sveen, Y. Guo, P. A. Davies, and J. Grue, On the breaking of internal solitary waves at a ridge, J. Fluid Mech. **469**, 161 (2002).

[20] V. I. Vlasenko and K. Hutter, Generation of second mode solitary waves by the interaction of a first mode soliton with a sill, Nonlinear Processes in Geophys. **8**, 223 (2001).

[21] K. G. Lamb and A. Warn-Varnas, Two-dimensional numerical simulations of shoaling internal solitary waves at the ASIAEX site in the South China Sea, Nonlinear Processes Geophys. **22**, 289 (2015).

[22] Y.-H. Wang, C.-F. Dai, and Y.-Y. Chen, Physical and ecological processes of internal waves on an isolated reef ecosystem in the South China Sea, Geophys. Res. Lett. **34**, L18609 (2007).

[23] K. G. Lamb and W. Xiao, Internal solitary waves shoaling onto a shelf: Comparisons of weakly-nonlinear and fully nonlinear models for hyperbolic-tangent stratifications, Ocean Model. **78**, 17 (2014).

[24] T. Gerkema, Development of internal solitary waves in various thermocline regimes—a multi-modal approach, Nonlinear Processes Geophys. **10**, 397 (2003).

[25] J. Olsthoorn, A. Baglaenko, and M. Stastna, Analysis of asymmetries in propagating mode-2 waves, Nonlinear Processes Geophys. **20**, 59 (2013).

[26] Y. Guo, J. K. Sveen, P. A. Davies, J. Grue, and P. Dong, Modelling the motion of an internal solitary wave over a bottom ridge in a stratified fluid, Environ. Fluid Mech. **4**, 415 (2004).
[27] T. B. Benjamin, Internal waves of permanent form in fluids of great depth, J. Fluid Mech. **29**, 559 (1967).
[28] C. J. Subich, K. G. Lamb, and M. Stastna, Simulation of the Navier-Stokes equations in three dimensions with a spectral collocation method, Int. J. Numerical Methods Fluids **73**, 103 (2013).
[29] http://www.sharcnet.ca
[30] T. Maxworthy, Experiments on solitary internal Kelvin waves, J. Fluid Mech. **129**, 365 (1983).
[31] R. Grimshaw, E. Pelinovsky, and T. Talipova, Fission of a weakly nonlinear interfacial solitary wave at a step, Geophys. Astrophys. Fluid Dyn. **102**, 179 (2008).
[32] K. G. Lamb and V. T. Nguyen, Calculating energy flux in internal solitary waves with an application to reflectance, J. Phys. Oceanogr. **39**, 559 (2009).